COGENT

R. Cohen, P. Colella, M. Dorf, M. Dorr, D. Ghosh,
J. Hittinger, D. Martin, P. McCorquodate, C. Reynolds,
T. Rognlien, P. Schwartz

LLNL-SM-689837

March 30, 2016

[1]

1 Introduction

The purpose of this document is to provide an overview of the COGENT (COntinuum Gyrokinetic Edge New Technology) code [5,8–13]. COGENT is being developed as part of a multidisciplinary collaboration called the Edge Simulation Laboratory (ESL) [20], involving the DOE Office of Advanced Scientific Computing Applied Mathematics Research Program and the Office of Fusion Energy Sciences Theory Program.

As described in the subsequent sections, COGENT solves a system of equations describing the behavior of plasma in the edge region of a tokamak fusion reactor. The ability to model computationally the behavior of such edge plasmas is a key element in the development of a predictive simulation capability. Among the features that distinguish the edge from the plasma core is the development of a region of steep gradients in the density and temperature profiles called the pedestal, the height of which determines the quality of plasma confinement, and hence fusion gain. A kinetic plasma model is needed in this region because the radial width of the pedestal observed in experiments is comparable to the radial width of individual particle orbits. These commensurate scales lead to large distortions of the local distribution functions from a Maxwellian. In addition, the mean free path can be comparable to the scale length for temperature variations along the magnetic field, which violates the assumptions underlying a collisional fluid model.

A variety of computational challenges arise in the development of a continuum kinetic edge model, including efficient discretization in a high-dimensional and complicated phase

[1]This material is based upon work supported by the U.S. Department of Energy, Office of Science, Office of Advanced Scientific Computing Research, Applied Mathematics program under contract number DE-AC52-07NA27344.

space, long-time integration with low numerical dissipation, conservation, preservation of distribution function positivity, strong anisotropy, and multiple spatial and temporal scales. To address these challenges in a comprehensive fashion, several numerical methodologies have been developed and deployed in COGENT. COGENT has therefore served as a testbed for these new techniques, as well as a platform for the development of a new edge plasma simulation tool.

2 Models

COGENT solves a model system defined by electrostatic, gyrokinetic Vlasov-Poisson equations in gyrocenter coordinates. These equations describe the coupled evolution of a gyrocenter distribution function f and an electrostatic potential function Φ under the influence of a large, imposed magnetic field $\mathbf{B}$. The use of gyrocenter coordinates provides two major advantages: particle gyromotion, that is the gyration of particles about the magnetic field, decouples from the remaining particle dynamics and the gyrocenter coordinate system is derived as a symplectic mapping from laboratory coordinates. A consequence of the former is that it reduces the dimension of the phase space domain on which the distribution function is defined and eliminates unimportant high-frequency modes from the simulation. The latter ensures that phase space volumes, and hence conservation properties, are preserved.

The electrostatic, gyrokinetic Vlasov-Poisson equations are a subset of more general electromagnetic models suitable for applications such as tokamak edge plasmas. Applied to complex geometric domains, the electrostatic model system exhibits many important numerical difficulties common with more general models, so it serves as a sensible starting point. An expectation is that this work will be extended to more complete physical models.

2.1 Gyrokinetic Vlasov equation

The gyrokinetic Vlasov equation describes the evolution of a scalar-valued positive-definite distribution function f defined over a five-dimensional phase space. For a magnetic field with magnitude $B = |\mathbf{B}|$, the gyrocenter phase space coordinates are denoted by the tuple $(\mathbf{R}, v_\parallel, \mu)$, where $\mathbf{R} \in \mathbb{R}^3$ is the position coordinate, $\mu \equiv \frac{1}{2} m v_\perp^2 / B \geq 0$ is the magnetic moment, $v_\perp$ and $v_\parallel$ are the velocity components perpendicular and parallel to the magnetic field $\mathbf{B}$, respectively, and m is the particle mass. The magnetic moment μ is preferred as a coordinate over $v_\perp$ because it is a constant of the motion, that is, $\dot{\mu} = 0$. Assuming that the gyrocenter distribution function for species α, $f_\alpha(\mathbf{R}, v_\parallel, \mu, t)$, is symmetric in the gyrophase θ, the corresponding Vlasov equation is therefore

$$\frac{df_\alpha}{dt} = \frac{\partial f_\alpha}{\partial t} + \dot{\mathbf{R}}_\alpha \cdot \boldsymbol{\nabla}_{\mathbf{R}} f_\alpha + \dot{v}_{\parallel\alpha} \frac{\partial f_\alpha}{\partial v_\parallel} = 0, \tag{1}$$

where $\boldsymbol{\nabla}_{\mathbf{R}}$ denotes the gradient with respect to $\mathbf{R}$. In a perturbative ordering suitable for large electric field gradients [16, 19],

$$\dot{\mathbf{R}}_\alpha \equiv \dot{\mathbf{R}}_\alpha(\mathbf{R}, v_\parallel, \mu, t) \equiv \frac{v_\parallel}{B_{\parallel_\alpha}^*}\mathbf{B}_\alpha^* + \frac{1}{Z_\alpha e B_{\parallel_\alpha}^*}\mathbf{b}\times\mathbf{G}_\alpha, \tag{2}$$

$$\dot{v_{\parallel}}_\alpha \equiv \dot{v_{\parallel}}_\alpha(\mathbf{R}, v_\parallel, \mu, t) \equiv -\frac{1}{m_\alpha B_{\parallel_\alpha}^*}\mathbf{B}_\alpha^*\cdot\mathbf{G}_\alpha, \tag{3}$$

where e is the fundamental charge, $\mathbf{b} \equiv \mathbf{b}(\mathbf{R}) \equiv \mathbf{B}/B$,

$$\mathbf{B}_\alpha^* \equiv \mathbf{B}_\alpha^*(\mathbf{R}, v_\parallel) \equiv \mathbf{B} + \frac{m_\alpha}{Z_\alpha e}\boldsymbol{\nabla}_{\mathbf{R}}\times\left(\mathbf{u} + v_\parallel\mathbf{b}\right), \tag{4}$$

and $\mathbf{u} \equiv \mathbf{u}(\mathbf{R}) \equiv \mathbf{b}\times\boldsymbol{\nabla}_{\mathbf{R}}\Phi_0/B$ for the equilibrium potential $\Phi_0 \equiv \Phi_0(\mathbf{R})$. The vector function $\mathbf{G}_\alpha$ depends on the magnetic and potential fields:

$$\mathbf{G}_\alpha \equiv \mathbf{G}_\alpha(\mathbf{R}, \mu, t) \equiv Z_\alpha e\boldsymbol{\nabla}_{\mathbf{R}}\Phi + \mu\boldsymbol{\nabla}_{\mathbf{R}}B + \frac{\mu B}{2\Omega_\alpha}\boldsymbol{\nabla}_{\mathbf{R}}\left(\mathbf{b}\cdot\boldsymbol{\nabla}_{\mathbf{R}}\times\mathbf{u}\right) + \frac{m_\alpha}{2}\boldsymbol{\nabla}_{\mathbf{R}}\left(u^2\right), \tag{5}$$

where Ω_α is the gyrofrequency and

$$\Phi \equiv \Phi(\mathbf{R}, t) \equiv \Phi_0 + \delta\Phi, \tag{6}$$

where $\delta\Phi \equiv \delta\Phi(\mathbf{R}, t)$. In these equations, we are assuming that all of the fields have been evaluated at gyrocenter coordinates via gyroaveraging from their native lab frame coordinates. Note that if we assume $\Phi_0 \equiv 0$, as we should in the initial implementation, then

$$\mathbf{B}_\alpha^* \equiv \mathbf{B}_\alpha^*(\mathbf{R}, v_\parallel) \equiv \mathbf{B} + \frac{m_\alpha v_\parallel}{Z_\alpha e}\boldsymbol{\nabla}_{\mathbf{R}}\times\mathbf{b}, \tag{7}$$

and

$$\mathbf{G}_\alpha \equiv \mathbf{G}_\alpha(\mathbf{R}, \mu, t) \equiv Z_\alpha e\boldsymbol{\nabla}_{\mathbf{R}}\Phi + \mu\boldsymbol{\nabla}_{\mathbf{R}}B. \tag{8}$$

Due to the phase space divergence free condition

$$\boldsymbol{\nabla}_{\mathbf{R}}\cdot\left(B_{\parallel_\alpha}^*\dot{\mathbf{R}}_\alpha\right) + \frac{\partial}{\partial v_\parallel}\left(B_{\parallel_\alpha}^*\dot{v_{\parallel}}_\alpha\right) = 0, \tag{9}$$

where $B_{\parallel_\alpha}^* \equiv B_{\parallel_\alpha}^*(\mathbf{R}, v_\parallel) \equiv \mathbf{B}_\alpha^*\cdot\mathbf{b}$, the gyrokinetic Vlasov equation (1) can be written in conservation form as

$$\frac{\partial(B_{\parallel_\alpha}^* f_\alpha)}{\partial t} + \boldsymbol{\nabla}_{\mathbf{R}}\cdot\left(\dot{\mathbf{R}}_\alpha B_{\parallel_\alpha}^* f_\alpha\right) + \frac{\partial}{\partial v_\parallel}\left(\dot{v_{\parallel}}_\alpha B_{\parallel_\alpha}^* f_\alpha\right) = 0. \tag{10}$$

2.2 Gyrokinetic Poisson equation

The potential Φ in the factors $\dot{\mathbf{R}}$ and $\dot{v_\parallel}$ in (2) and (3) is obtained by solving the Poisson equation

$$\epsilon_0 \boldsymbol{\nabla}^2 \Phi(x,t) = e\left(n_e(x,t) - \sum_\alpha Z_\alpha n_\alpha(x,t) \right) \tag{11}$$

in the laboratory coordinates x, then gyroaveraging to gyrocenter coordinates. The electron and ion charge densities n_e and n_α in (11) are related to the velocity space integrals of the respective particle distribution functions. At this stage of the development, let us assume that n_e is known. Due to the finite gyroradius effects, the zeroth moment of the ion gyrocenter distribution function is fairly complicated [14]. In general, it has two contributions:

$$n_\alpha = \bar{n}_\alpha + \hat{n}_\alpha. \tag{12}$$

The first term is the *gyrocenter density*

$$\bar{n}_\alpha \equiv \bar{n}_\alpha(x,t) \equiv \frac{1}{m_\alpha} \int f_\alpha(\mathbf{R}, v_\parallel, \mu, t) \delta(\mathbf{R} - x + \boldsymbol{\rho}_\alpha(\theta)) B^*_\parallel(\mathbf{R}, v_\parallel) d\mathbf{R} dv_\parallel d\mu d\theta \tag{13}$$

that is the density at point x from contributions of "rings of density" about gyrocenters $\mathbf{R}$ at distances $\rho_\alpha = |\boldsymbol{\rho}_\alpha|$ from x (the θ integral distributes the particle density uniformly around the ring $\boldsymbol{\rho}_\alpha(\theta)$). In the long wavelength limit, $k_\perp \rho_\alpha \ll 1$, where $k_\perp$ is the perpendicular wavenumber of the magnetic field and $\rho_\alpha = v_\perp / \Omega_\alpha$ is the cyclotron radius, this simplifies to

$$\begin{aligned} \bar{n}_\alpha(x,t) &\approx \frac{2\pi}{m_\alpha} \int \left(f_\alpha(x, v_\parallel, \mu, t) + \frac{\rho_\alpha^2}{2} \boldsymbol{\nabla}^2_\perp f_\alpha(x, v_\parallel, \mu, t) \right) B^*_\parallel(x, v_\parallel) dv_\parallel d\mu \\ &= n_{\alpha,gc}(x,t) + \frac{1}{\Omega^2_\alpha(x)} \boldsymbol{\nabla}^2_\perp p_{\alpha,\perp}(x,t). \end{aligned} \tag{14}$$

where

$$n_{\alpha,gc}(x,t) \equiv \frac{2\pi}{m_\alpha} \int f_\alpha(x, v_\parallel, \mu, t) B^*_\parallel(x, v_\parallel) dv_\parallel d\mu, \tag{15}$$

$$p_{\alpha,\perp}(x,t) \equiv \frac{2\pi B(x)}{m_\alpha^2} \int \mu f_\alpha(x, v_\parallel, \mu, t) B^*_\parallel(x, v_\parallel) dv_\parallel d\mu, \tag{16}$$

$$\Omega_\alpha(x) \equiv \frac{Z_\alpha e B(x)}{m_\alpha}. \tag{17}$$

The second term in (12) is the *polarization density*, which is the gyrophase-dependent contribution. In the long wavelength limit, the gyrokinetic Poisson equation takes the form [19] (adding a missing Z_α factor)

$$\epsilon_0 \boldsymbol{\nabla}^2 \Phi = e\left(n_e - \sum_\alpha Z_\alpha \bar{n}_\alpha \right) - e^2 \sum_\alpha \frac{Z_\alpha^2}{m_\alpha \Omega^2_\alpha} \boldsymbol{\nabla}_\perp \cdot \left(\bar{n}_\alpha \boldsymbol{\nabla}_\perp \Phi \right), \tag{18}$$

where $\boldsymbol{\nabla}_\perp \equiv \boldsymbol{\nabla} - \mathbf{b}(\mathbf{b}\cdot\boldsymbol{\nabla})$ is the component of $\boldsymbol{\nabla}$ perpendicular to $\mathbf{B}$. Expressed in flux divergence form, we have

$$\boldsymbol{\nabla}\cdot\left\{\left[\epsilon_0\mathbf{I} + e^2\sum_\alpha \frac{Z_\alpha^2\bar{n}_\alpha}{m_\alpha\Omega_\alpha^2}\left(\mathbf{I}-\mathbf{b}\mathbf{b}^T\right)\right]\boldsymbol{\nabla}\Phi\right\} = e\left(n_e - \sum_\alpha Z_\alpha\bar{n}_\alpha\right), \tag{19}$$

where we have employed the long wavelength limit assumption to commute $1/\Omega_\alpha^2$ with $\boldsymbol{\nabla}_\perp$.

2.3 Adiabatic electron model

In our discretization of the Vlasov-Poisson model, we are assuming a smooth mapping $\mathbf{X}$ from the unit cube computational domain onto the physical spatial domain Ω

$$\mathbf{X} = \mathbf{X}(\xi),\ \mathbf{X} : [0,1]^3 \to \Omega. \tag{20}$$

Let us further assume that the first coordinate ξ_1 labels flux surfaces. For our initial implementation, we will assume an adiabatic model for the electrons.

$$n_e(x) = n_0(\xi_1(x))\exp\left(\frac{e\Phi(x)}{T_e(\xi_1(x))}\right), \tag{21}$$

where, as indicated, the prefactor n_0 and temperature T_e are functions of the flux surface label. To maintain charge neutrality within a flux surface, the prefactor n_0 will equated to the ion flux-surface averaged density (summed over species with the appropriate ionization state weights). The electron temperature can be set arbitrarily. This procedure accomplishes the desired result if the flux surface average of the Boltzmann (exponential) factor is unity.

Another variation of the adiabatic electron model divides by the flux surface average of the Boltzmann exponent as part of the prefactor:

$$n_e(x) = n_0(\xi_1(x))\frac{\exp\left(\frac{e\Phi(x)}{T_e(\xi_1(x))}\right)}{\left\langle\exp\left(\frac{e\Phi(x)}{T_e(\xi_1(x))}\right)\right\rangle}, \tag{22}$$

If now n_0 is equated to the ion flux-surface averaged density, then charge neutrality within a flux surface is maintained for an arbitrary average of the Boltzmann factor. There are other possible variations; for example the averages can be taken over the entire simulation volume to describe global charge conservation with rapid electron transport in all directions.

2.4 Collisions

Since collisions become increasingly important in the outer edge of a tokamak plasma, we must include their effect in our numerical model and discretization strategy. The Vlasov

equation (10) can be further generalized to a Boltzmann equation by the inclusion of a collision term in the right hand side

$$\frac{\partial(B_\parallel^* f_i)}{\partial t} + \bar{\nabla} \cdot \left(\frac{d\bar{\mathbf{R}}}{dt} B_\parallel^* f_i \right) + \frac{\partial}{\partial \bar{v}_\parallel} \left(\frac{d\bar{v}_\parallel}{dt} B_\parallel^* f_i \right) = C(f_i, f_i). \tag{23}$$

A general category of collision model is described by Fokker-Planck operators, which in laboratory coordinates have the form [4]

$$C(f_i, f_i) \equiv -\Gamma \frac{\partial}{\partial v} \cdot \left[f_i \frac{\partial H}{\partial v} - \frac{1}{2} \frac{\partial}{\partial v} \cdot \left(\frac{\partial^2 G}{\partial v \partial v} f_i \right) \right], \tag{24}$$

where $v = (v_\parallel, v_\perp)$. The quantity $\Gamma \equiv 4\pi Z_i^4 \lambda / m_i^2$ where λ is the Coulomb logarithm and Z_i is the charge state. In the case of a linear collision operator, the friction and diffusion coefficients H and G are prescribed functions independent of f_i. In the nonlinear case, these functions are the *Rosenbluth potentials*, which are the solutions of a pair of potential equations in velocity space involving f_i.

As described in [4], numerical discretizations of Fokker-Planck operators (24) can be constructed so as to obtain conservation of mass, momentum and energy. The fact that (24) is posed as the divergence of a flux plays an important role in establishing these properties, although in the case of energy conservation this fact in itself is not sufficient (as it is for mass conservation). Since (23) is posed in gyrocenter, not laboratory, coordinates, the question therefore arises as to what happens when a Fokker-Planck collision operator is transformed to these coordinates. This question is addressed in [3] in which a Poisson bracket formalism is used to obtain a transformed Fokker-Planck collision operator in gyrocenter coordinates

$$C(f_i, f_i) = -\frac{1}{\mathcal{J}} \frac{\partial}{\partial Z} \left[\mathcal{J} \left(\mathcal{K} F_i - \mathcal{D} \frac{\partial F_i}{\partial Z} \right) \right] \tag{25}$$

where $\mathcal{J}$ denotes the Jacobian of the mapping $\mathcal{T}$ of laboratory phase space coordinates z to gyrocenter coordinates $Z = \mathcal{T} z$, and $F_i \equiv \mathcal{T}^{-1} f_i$ denotes the *push-forward* of f_i generated by $\mathcal{T}$. The operator (25) has a similar form as (24) in the sense that it is the sum of a drag term (with coefficient $\mathcal{K}$) and a diffusion term (with coefficient $\mathcal{D}$). Unlike (24), in which the drag and diffusion operators act solely in velocity space, the analogous operators of (25) involve spatial derivatives. This is simply due to the mixing of spatial and velocity phase space components resulting from gyroaveraging. Therefore, while the divergence form of (25) provides the apparent opportunity for enforcing conservation in a numerical formulation, it does not automatically follow from the prior work of [4]. In this project, we must re-investigate these conservation questions in the overall numerical discretization of (23).

2.5 Normalizations

Our implementation of the gyrokinetic Vlasov-Poisson system will employ normalizations relative to a reference material and fields described by the parameters specified in Table 1.

$\widetilde{n}$	number density
$\widetilde{T}$	temperature
$\widetilde{L}$	length
$\widetilde{m}$	mass
$\widetilde{B}$	magnetic field

Table 1: Primitive reference parameters.

$\widetilde{v} \equiv \left(\widetilde{T}/\widetilde{m}\right)^{1/2}$	thermal speed
$\widetilde{\tau} \equiv \widetilde{L}/\widetilde{v}$	transit time
$\widetilde{\mu} \equiv \widetilde{T}/(2\widetilde{B})$	magnetic moment
$\widetilde{f} \equiv \widetilde{n}/(\pi\widetilde{v}^3)$	distribution function
$\widetilde{\Phi} \equiv \widetilde{T}/e$	potential
$\widetilde{\Omega} \equiv e\widetilde{B}/\widetilde{m}$	gyrofrequency
$\widetilde{\lambda}_D \equiv \left(\epsilon_0\widetilde{T}/(\widetilde{n}e^2)\right)^{1/2}$	Debye length

Table 2: Derived reference parameters.

These choices then determine the set of derived reference quantities shown in Table 2. In terms of these parameters, the normalized variables to be used in the gyrokinetic Vlasov-Poisson model are displayed in Table 3. From the reference scales, two dimensionless numbers can be constructed that appear in the gyrokinetic Vlasov-Poisson system; these are defined in Table 4.

2.6 Normalized gyrokinetic Vlasov equations

We now apply the above normalizations to gyrokinetic Vlasov equations in Section 2.1. For simplicity, we will deglect the drift due to the equilibrium potential (*i.e.*, we assume $\mathbf{u} = 0$). We obtain

$$\frac{\partial(\widehat{B_{\parallel}}^*_\alpha \widehat{f}_\alpha)}{\partial \widehat{t}} + \boldsymbol{\nabla}_{\widehat{\mathbf{R}}} \cdot \left(\dot{\widehat{\mathbf{R}}}_\alpha \widehat{B_{\parallel}}^*_\alpha \widehat{f}_\alpha\right) + \frac{\partial}{\partial \widehat{v}_\parallel}\left(\dot{\widehat{v}}_{\parallel\alpha} \widehat{B_{\parallel}}^*_\alpha \widehat{f}_\alpha\right) = 0, \tag{26}$$

where

$$\dot{\widehat{\mathbf{R}}}_\alpha \equiv \dot{\widehat{\mathbf{R}}}_\alpha(\widehat{\mathbf{R}}, \widehat{v}_\parallel, \widehat{\mu}, \widehat{t}) \equiv \frac{\widehat{v}_\parallel}{\widehat{B_{\parallel}}^*_\alpha}\widehat{\mathbf{B}}^*_\alpha + \frac{La}{Z_\alpha \widehat{B_{\parallel}}^*_\alpha}\mathbf{b} \times \widehat{\mathbf{G}}_\alpha, \tag{27}$$

$$\dot{\widehat{v}}_{\parallel\alpha} \equiv \dot{\widehat{v}}_{\parallel\alpha}(\widehat{\mathbf{R}}, \widehat{v}_\parallel, \widehat{\mu}, \widehat{t}) \equiv -\frac{1}{\widehat{m}_\alpha \widehat{B_{\parallel}}^*_\alpha}\widehat{\mathbf{B}}^*_\alpha \cdot \widehat{\mathbf{G}}_\alpha, \tag{28}$$

$\widehat{t} \equiv t/\widetilde{\tau}$	time
$\widehat{v}_\parallel \equiv v_\parallel/\widetilde{v}$	parallel velocity
$\widehat{n}_\alpha \equiv n_\alpha/\widetilde{n}$	number density
$\widehat{m}_\alpha \equiv m_\alpha/\widetilde{m}$	mass
$\widehat{f}_\alpha \equiv f_\alpha/\widetilde{f}$	distribution function
$\widehat{T}_\alpha \equiv T_\alpha/\widetilde{T}$	temperature
$\widehat{B} \equiv B/\widetilde{B}$	magnetic field
$\widehat{\Phi} \equiv \Phi/\widetilde{\Phi}$	potential
$\widehat{\mu} \equiv \mu/\widetilde{\mu}$	magnetic moment

Table 3: Normalized gyrokinetic Vlasov-Poisson variables.

$La \equiv \widetilde{v}/(\widetilde{\Omega}\widetilde{L})$	Larmor number: ratio of gyroradius to scale length
$De \equiv \widetilde{\lambda}_D/\widetilde{L}$	Debye number: ratio of Debye length to scale length

Table 4: Dimensionless gyrokinetic Vlasov-Poisson parameters.

and

$$\widehat{\mathbf{B}}^*_\alpha \equiv \widehat{\mathbf{B}}^*_\alpha(\widehat{\mathbf{R}}, \widehat{v}_\parallel) \equiv \widehat{\mathbf{B}} + La\frac{\widehat{m}_\alpha \widehat{v}_\parallel}{Z_\alpha}\boldsymbol{\nabla}_{\widehat{\mathbf{R}}} \times \mathbf{b}, \tag{29}$$

$$\widehat{B_\parallel}^*_\alpha \equiv \widehat{B_\parallel}^*_\alpha(\widehat{\mathbf{R}}, \widehat{v}_\parallel) \equiv \mathbf{b} \cdot \widehat{\mathbf{B}}^*_\alpha, \tag{30}$$

$$\widehat{\mathbf{G}}_\alpha \equiv \widehat{\mathbf{G}}_\alpha(\widehat{\mathbf{R}}, \widehat{\mu}, \widehat{t}) \equiv Z_\alpha \boldsymbol{\nabla}_{\widehat{\mathbf{R}}}\widehat{\Phi} + \frac{\widehat{\mu}}{2}\boldsymbol{\nabla}_{\widehat{\mathbf{R}}}\widehat{B}. \tag{31}$$

2.7 Normalized gyrokinetic Poisson equation

Applying the above normalizations, we obtain from (19)

$$\boldsymbol{\nabla}_{\widehat{\mathbf{X}}} \cdot \left\{ \left[(De)^2 \mathbf{I} + (La)^2 \sum_\alpha \frac{Z_\alpha^2 \widehat{\bar{n}}_\alpha}{\widehat{m}_\alpha \widehat{\Omega}_\alpha^2} \left(\mathbf{I} - \mathbf{b}\mathbf{b}^T \right) \right] \boldsymbol{\nabla}_{\widehat{\mathbf{X}}} \widehat{\Phi} \right\} = \widehat{n}_e - \sum_\alpha Z_\alpha \widehat{\bar{n}}_\alpha, \tag{32}$$

where $\boldsymbol{\nabla}_{\widehat{\mathbf{X}}}$ denotes the gradient with respect to the normalized spatial coordinate $\widehat{\mathbf{X}} \equiv \mathbf{X}/\widetilde{L}$.

2.8 Normalized adiabatic electron model

Applying the above normalizations, we obtain from (21)

$$\widehat{n}_e(x) = \widehat{n}_0(\xi_1(x)) \exp\left(\frac{\widehat{\Phi}(x)}{\widehat{T}_e(\xi_1(x))} \right). \tag{33}$$

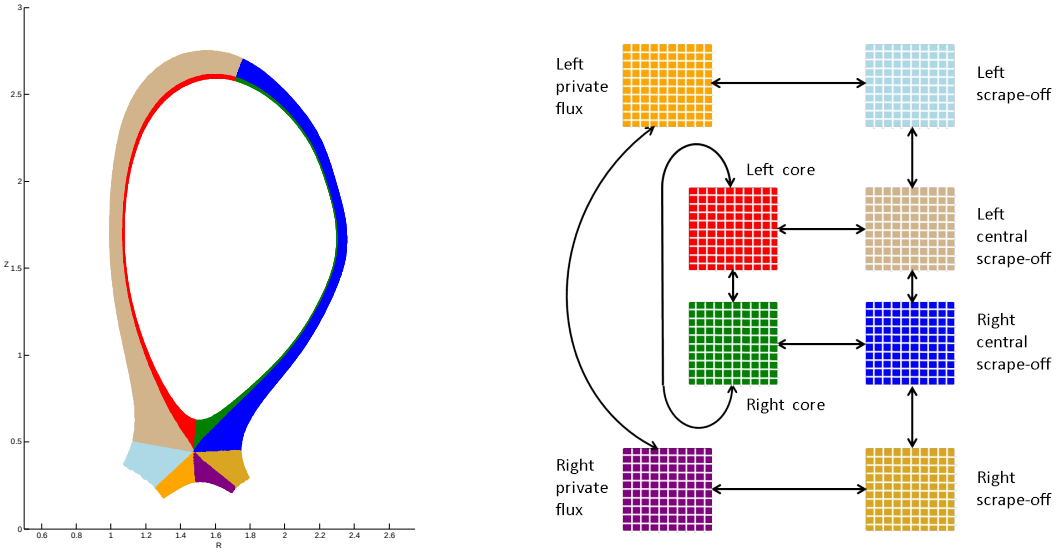

Figure 1: Edge plasma geometry (left) and multiblock, locally rectangular computational domain (right). Arrows indicate the inter-block connectivity.

and from (22) the alternate model

$$\widehat{n}_e(x) = \widehat{n}_0(\xi_1(x)) \frac{\exp\left(\dfrac{\widehat{\Phi}(x)}{\widehat{T}_e(\xi_1(x))}\right)}{\left\langle \exp\left(\dfrac{\widehat{\Phi}(x)}{\widehat{T}_e(\xi_1(x))}\right)\right\rangle}. \tag{34}$$

3 Geometry

The gyrokinetic Vlasov-Poisson system described in the preceding sections is posed in a domain defined by the tokamak magnetic geometry, which is comprised of field lines lying on concentric flux surfaces. Due to large variations of plasma parameters along and across field lines, there is strong motivation to discretize in coordinates where one of the coordinate directions is defined by the flux surfaces. As depicted in Figure 1, a natural choice is a *mapped multiblock* coordinate system, where the blocks correspond to the logically distinct core, scrape-off layer and private flux regions. Within each block, a rectangular coordinate system can be employed, which facilitates efficient and accurate discretizations and domain decompositions over processors.

COGENT also provides the option to use a simpler single-block geometry, such as that shown in Figure 2, based on the well-known Miller equilibrium model [18]. COGENT results obtained using this geometry in the prediction of geodesic acoustic modes are contained in [11] and [9].

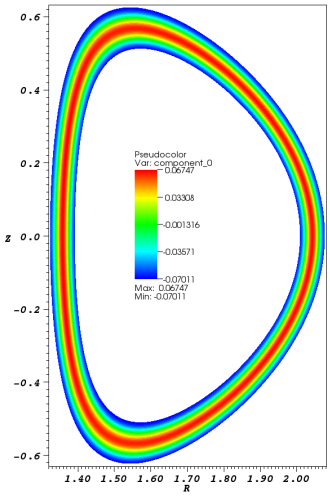

Figure 2: COGENT computed potential in Miller equilibrium geometry.

4 Boundary conditions

In this section, we describe the imposition of phase space boundary conditions in terms of the configuration space computational coordinates $\xi = (\xi_1, \xi_2) \in [0,1]^2$ and a velocity space domain defined by

$$\Omega_v \equiv \left\{ (v_\parallel, \mu) : v_{\parallel,\min} \le v_\parallel \le v_{\parallel,\max},\ \mu_{\min} \le \mu \le \mu_{\max} \right\}. \tag{35}$$

4.1 Vlasov

4.1.1 Phase space inflow

Given the advection fluxes in (26), a natural way to specify boundary conditions is based on the directions of the phase space velocities $\dot{\widehat{\mathbf{R}}}$ and $\dot{\widehat{v}}_\parallel$ at boundaries. For the configuration space flux at radial boundaries, we specify

$$\dot{\widehat{\mathbf{R}}} \widehat{B}_\parallel^* \widehat{f}(\xi_1, \xi_2, v_\parallel, \mu) = \begin{cases} \Gamma_{\mathbf{R}} & \text{if } \dot{\widehat{\mathbf{R}}} \cdot \mathbf{n}_{\widehat{\mathbf{R}}} < 0, \\ 0 & \text{if } \dot{\widehat{\mathbf{R}}} \cdot \mathbf{n}_{\widehat{\mathbf{R}}} \ge 0, \end{cases} \qquad \begin{array}{l} \xi_1 = 0 \text{ or } 1,\ 0 \le \xi_2 \le 1, \\ (v_\parallel, \mu) \in \Omega_v, \end{array} \tag{36}$$

where $\mathbf{n}_{\widehat{\mathbf{R}}}$ is the outward pointing unit normal. Similarly, at the lower $v_\parallel$ boundary

$$\dot{\widehat{v}}_\parallel \widehat{B}_\parallel^* \widehat{f}(\xi_1, \xi_2, v_\parallel, \mu) = \begin{cases} \Gamma_{v_\parallel}^{lower} & \text{if } \dot{\widehat{v}}_\parallel > 0, \\ 0 & \text{if } \dot{\widehat{v}}_\parallel \le 0, \end{cases} \qquad \begin{array}{l} 0 \le \xi_1, \xi_2 \le 1, \\ v_\parallel = v_{\parallel,\min},\ \ \mu_{\min} \le \mu \le \mu_{\max}, \end{array} \tag{37}$$

and at the upper $v_\parallel$ boundary

$$\dot{\widehat{v}_\parallel}\widehat{B}_\parallel^*\widehat{f}(\xi_1,\xi_2,v_\parallel,\mu) = \begin{cases} \Gamma_{v_\parallel}^{upper} & \text{if } \dot{\widehat{v}_\parallel} < 0, \qquad 0 \le \xi_1,\xi_2 \le 1, \\ 0 & \text{if } \dot{\widehat{v}_\parallel} \ge 0, \qquad v_\parallel = v_{\parallel,\max}, \quad \mu_{\min} \le \mu \le \mu_{\max}. \end{cases} \tag{38}$$

4.1.2 Periodic

A periodic boundary may be imposed on radial boundaries radial coordinate

$$\widehat{f}(0,\xi_2,v_\parallel,\mu) = \widehat{f}(1,\xi_2,v_\parallel,\mu), \quad 0 \le \xi_2 \le 1,\ (v_\parallel,\mu) \in \Omega_v, \tag{39}$$

or the poloidal boundary

$$\widehat{f}(\xi_1,0,v_\parallel,\mu) = \widehat{f}(\xi_1,1,v_\parallel,\mu), \quad 0 \le \xi_1 \le 1,\ (v_\parallel,\mu) \in \Omega_v. \tag{40}$$

4.2 Poisson

For the gyrokinetic Poisson equation (32), we impose Dirichlet, Neumann or periodic boundary conditions.

4.2.1 Dirichlet

A Dirichlet boundary condition may be imposed on mapped boundaries, *e.g.*,

$$\widehat{\Phi}(0,\xi_2) = \widehat{\Phi}^*, \quad 0 \le \xi_2 \le 1, \tag{41}$$

or

$$\widehat{\Phi}(1,\xi_2) = \widehat{\Phi}^*, \quad 0 \le \xi_2 \le 1, \tag{42}$$

for a prescribed boundary value $\widehat{\Phi}^*$.

4.2.2 Neumann

A Neumann boundary condition may be imposed on mapped boundaries, *e.g.*,

$$-\frac{\partial\widehat{\Phi}(0,\xi_2)}{\partial\xi_1} = \widehat{\Phi}^*(\xi_2), \quad 0 \le \xi_2 \le 1, \tag{43}$$

or

$$\frac{\partial\widehat{\Phi}(1,\xi_2)}{\partial\xi_1} = \widehat{\Phi}^*(\xi_2), \quad 0 \le \xi_2 \le 1, \tag{44}$$

for a prescribed boundary value $\widehat{\Phi}^*$. Note that we follow the usual convention of specifying "outward normal" derivatives.

4.2.3 Periodic

A periodic boundary may be imposed on mapped boundaries, *e.g.*,

$$\widehat{\Phi}(0,\xi_2) = \widehat{\Phi}(1,\xi_2), \quad 0 \le \xi_2 \le 1. \tag{45}$$

5 Discretization and numerical methods

Fundamental to COGENT has been the development of a formalism for generating high-order, finite-volume discretizations in mapped coordinate systems [6]. Given a smooth mapping $\boldsymbol{X} = \boldsymbol{X}(\boldsymbol{\xi})$, $\boldsymbol{X} : [0,1]^D \to \Omega$ from the unit cube (which ultimately serves as the computational domain) onto the spatial domain $\Omega \subset \mathbb{R}^D$, the integral of the divergence of a flux $\boldsymbol{F}$ over a mapped control volume $V_{\boldsymbol{i}} \subset [0,1]^D$ is computed to fourth-order accuracy as

$$\int\limits_{\boldsymbol{X}(V_{\boldsymbol{i}})} \boldsymbol{\nabla}_{\boldsymbol{x}} \cdot \boldsymbol{F} d\boldsymbol{x} = h^2 \sum_{d=1}^{D} \sum_{\pm=+,-} \pm F^d_{\boldsymbol{i}\pm\frac{1}{2}\boldsymbol{e}^d} + O(h^4), \tag{46}$$

where

$$F^d_{\boldsymbol{i}\pm\frac{1}{2}\boldsymbol{e}^d} \equiv \sum_{s=1}^{D} \langle N^s_d \rangle_{\boldsymbol{i}+\frac{1}{2}\boldsymbol{e}^d} \langle F^s \rangle_{\boldsymbol{i}+\frac{1}{2}\boldsymbol{e}^d} + \frac{h^2}{12} \sum_{s=1}^{D} \left(\boldsymbol{G}_0^{\perp,d} \langle N^s_d \rangle_{\boldsymbol{i}+\frac{1}{2}\boldsymbol{e}^d} \right) \cdot \left(\boldsymbol{G}_0^{\perp,d} (\langle F^s \rangle_{\boldsymbol{i}+\frac{1}{2}\boldsymbol{e}^d} \right). \tag{47}$$

Here, $\langle \cdot \rangle_{\boldsymbol{i}+\frac{1}{2}\boldsymbol{e}^d}$ denotes a fourth-order accurate cell face average and $\boldsymbol{G}_0^{\perp,d}$ is the second-order accurate central difference approximation to the component of the gradient operator orthogonal to the d-th direction. The quantities N^s_d are metric factors associated with the mapping $\boldsymbol{X}$. An important element is the calculation of the metric factor face averages $\langle N^s_d \rangle_{\boldsymbol{i}+\frac{1}{2}\boldsymbol{e}^d}$ in such a way as to preserve free streaming (*i.e.*, (46) vanishes when $\boldsymbol{F}$ is uniform) to machine roundoff. This improves stability by preventing roundoff error accumulation due to the discretization of the coordinate mapping. Complete details and applications to hyperbolic and elliptic operators are contained in [6].

To accommodate geometries such as that in Figure 1, we extend our approach by considering an arbitrary collection of mapped blocks. In our conservative formulation, the primary concern is the calculation of fluxes at interblock interfaces. Assuming that the smooth mappings on each block possess smooth extensions beyond their respective boundaries, "extrablock" ghost cells can be generated by applying the mapping to an extended computational grid (*e.g.*, Figure 3). Using a sufficiently accurate interpolation of valid data from neighboring blocks to fill the extrablock ghost cells, the flux at block boundaries can then be computed in the same manner as fluxes at cell faces in the block interior. The only special aspect of the interblock boundary flux calculation is a final averaging step that restores strict conservation. The key element is therefore the interpolation of valid neighbor block data to extrablock ghost cells, which is described in full detail in [17]. A polynomial interpolant is constructed in a neighborhood of the extrablock ghost cell whose coefficients

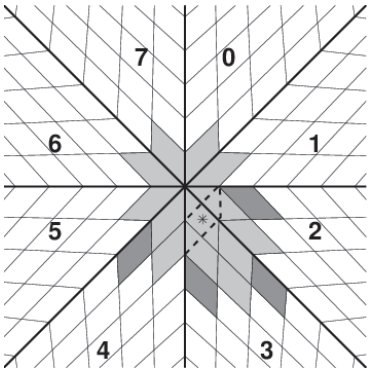

Figure 3: Extrablock ghost cell interpolation.

are constrained so as to ensure that cell averages of the interpolant agree with those in a neighboring set of cells (which may belong to one or more neighboring blocks). The coefficients are then obtained by solving a least-squares problem. The number of neighboring cells must be sufficiently large to obtain a system with maximal rank (determined by the desired interpolation order).

6 Software infrastructure

COGENT is implemented using the Chombo adaptive mesh refinement framework [7]. In addition to the support provided by Chombo for the fourth-order, mapped-multiblock, finite-volume discretization described in Section 5, COGENT utilizes Chombo's data containers for all mesh-dependent quantities distributed over processors. Communication (*e.g.*, the exchanging of ghost cell data) are effected by container members using MPI or via direct MPI calls (*e.g.*, to perform a global reduction). Distributed quantities are functions of configuration space (*e.g.*, potential) or phase space (*e.g.*, distribution functions), each of which can be domain-decomposed independently. Injection and projection operators between configuration/velocity and phase space have also been developed in COGENT. Although COGENT does not currently utilize Chombo's AMR capabilities, a future development path for this capability is nevertheless provided.

COGENT utilizes either *hypre* [15] or PETSc [21] to solve linear systems. In addition to Chombo, it is therefore necessary to download and build one of these libraries. The open-source VisIt visualization tool [2] is used to view a variety of plots created by COGENT in HDF5 format [1]. COGENT also used HDF5-formatted files for restarts (via Chombo), so it is necessary to have HDF5 installed in order to utilize either capability.

References

[1] HDF5 web site. `http://www.hdfgroup.org/HDF5/`.

[2] VisIt web site. http://www.llnl.gov/visit.

[3] A. J. Brizard. A guiding-center Fokker-Planck collision operator for nonuniform magnetic fields. *Phys. Plasmas*, 11(9):4429–4438, 2004.

[4] L. Chacon, D. C. Barnes, D. A. Knoll, and G. H. Miley. An implicit energy conservative 2d Fokker-Planck algorithm. i. difference scheme. *J. Comput. Phys.*, 157:618–653, 2000.

[5] R. H. Cohen, M. Dorf, and M. Dorr. Reduced electron models for edge simulation. *Contrib. Plasma Phys.*, 52(5–6):529–533, 2012.

[6] P. Colella, M. R. Dorr, J. A. F. Hittinger, and D. F. Martin. High-order, finite-volume methods in mapped coordinates. *J. Comput. Phys.*, 230:2952–2976, 2011.

[7] P. Colella, D. T. Graves, T. J. Ligocki, D. F. Martin, D. Modiano, D. B. Serafini, and B. Van Straalen. Chombo Software Package for AMR Applications - Design Document. http://seesar.lbl.gov/anag/chombo.

[8] M. A. Dorf, R. H. Cohen, J. C. Compton, M. Dorr, T. D. Rognlien, J. Angus, S. Krasheninnikov, P. Colella, D. Martin, and P. McCorquodale. Progress with the COGENT edge kinetic code: Collision operator options. *Contrib. Plasma Phys.*, 52(5–6):518–522, 2012.

[9] M. A. Dorf, R. H. Cohen, M. Dorr, T. Rognlien, J. Hittinger, J. Compton, P. Colella, D. Martin, and P. McCorquodale. Numerical modelling of geodesic acoustic mode relaxation in a tokamak edge. *Nucl. Fusion*, 53:063015, 2013.

[10] M. A. Dorf, M. R. Dorr, J. A. Hittinger, R. H. Cohen, and T. D. Roglien. Continuum kinetic modeling of the tokamak plasma edge. *Phys. Plasmas*, 23:056102–1 – 056102–12, 2016.

[11] M. R. Dorr, R. H. Cohen, P. Colella, M. A. Dorf, J. A. F. Hittinger, and D. F. Martin. Numerical simulation of phase space advection in gyrokinetic models of fusion plasmas. In *Proceedings of SciDAC 2010, Chattanooga, TN*, July 2010.

[12] M. R. Dorr, P. Colella, J. A. Hittinger, D. F. Martin, and P. W. McCorquodale. High resolution methods for phase space problems in complex geometries. In *Exascale Research Conference, Portland, OR, April 12-18*, 2012. http://exascaleresearch.labworks.org/apr2012/conference/materials#B76D3F23827C47EE988EA9820325AA9. Also available as Lawrence Livermore National Laboratory report LLNL-CONF-534497.

[13] M. R. Dorr, J. A. F. Hittinger, P. Colella, P. W. McCorquodale, R. H. Cohen, and M. A. Dorf. High-order discretization of a gyrokinetic vlasov model in edge plasma geometry. *J. Comput. Phys.*, 2013. In preparation.

[14] D. H. E. Dubin, J. A. Krommes, C. Oberman, and W. W. Lee. Nonlinear gyrokinetic equations. *Phys. Fluids*, 26:3524–3535, 1983.

[15] R. Falgout. Scalable linear solvers. `http://http://www.llnl.gov/CASC/hypre/software.html`.

[16] T. S. Hahm. Nonlinear gyrokinetic equations for turbulence in core transport barriers. *Phys. Plasmas*, 3(12):4658–4664, 1996.

[17] P. McCorquodale, M. R. Dorr, J. A. F. Hittinger, and P. Colella. High-order finite-volume methods for hyperbolic conservation laws on mapped multiblock grids. *J. Comput. Phys.*, 288:181–195, 2015.

[18] R. L. Miller, M. S. Chu, J. M. Greene, Y. R. Lin-Liu, and R. E. Waltz. Noncircular, finite aspect ratio, local equilibrium model. *Phys. Plasmas*, 5(4):973–978, 1998.

[19] H. Qin, R. H. Cohen, W. M. Nevins, and X. Q. Xu. General gyrokinetic equations for edge plasmas. *Plasma Phys. Contr. F.*, 2006. accepted.

[20] ESL web site. Edge simulation laboratory. `http:esl.lbl.gov/`.

[21] PETSc web site. Portable, extensible toolkit for scientific computation. `https://www.mcs.anl.gov/petsc/`.